Thickness dependence of the strain, band gap and transport properties of epitaxial In_2O_3 thin films grown on Y-stabilised ZrO_2(111)

2011 J. Phys.: Condens. Matter 23 334211

(http://iopscience.iop.org/0953-8984/23/33/334211)

J. Phys.: Condens. Matter **23** (2011) 334211 (8pp) doi:10.1088/0953-8984/23/33/334211

Thickness dependence of the strain, band gap and transport properties of epitaxial In_2O_3 thin films grown on Y-stabilised $ZrO_2(111)$

K H L Zhang[1], V K Lazarov[2,5], T D Veal[3], F E Oropeza[1], C F McConville[3], R G Egdell[1] and A Walsh[4]

[1] Department of Chemistry, Chemistry Research Laboratory, University of Oxford, Mansfield Road, Oxford OX1 3TA, UK
[2] Department of Materials, University of Oxford, Parks Road, Oxford OX1 3PH, UK
[3] Department of Physics, University of Warwick, Coventry CV4 7AL, UK
[4] Department of Chemistry, Kathleen Lonsdale Materials Chemistry, University College London, 20 Gordon Street, London WC1H 0AJ, UK

E-mail: Russell.egdell@chem.ox.ac.uk

Received 20 December 2010
Published 2 August 2011
Online at stacks.iop.org/JPhysCM/23/334211

Abstract

Epitaxial films of In_2O_3 have been grown on Y-stabilised $ZrO_2(111)$ substrates by molecular beam epitaxy over a range of thicknesses between 35 and 420 nm. The thinnest films are strained, but display a 'cross-hatch' morphology associated with a network of misfit dislocations which allow partial accommodation of the lattice mismatch. With increasing thickness a 'dewetting' process occurs and the films break up into micron sized mesas, which coalesce into continuous films at the highest coverages. The changes in morphology are accompanied by a progressive release of strain and an increase in carrier mobility to a maximum value of 73 $cm^2\ V^{-1}\ s^{-1}$. The optical band gap in strained ultrathin films is found to be smaller than for thicker films. Modelling of the system, using a combination of classical pair-wise potentials and *ab initio* density functional theory, provides a microscopic description of the elastic contributions to the strained epitaxial growth, as well as the electronic effects that give rise to the observed band gap changes. The band gap increase induced by the uniaxial compression is offset by the band gap reduction associated with the epitaxial tensile strain.

(Some figures in this article are in colour only in the electronic version)

1. Introduction

Transparent conducting oxides (TCOs) combine the properties of optical transparency in the visible region with a high electrical conductivity, and have widespread application as window electrodes in photovoltaic devices, liquid crystal displays and organic light emitting diodes [1]. At present, the materials used in technological situations are usually in the form of polycrystalline thin films deposited on glass or polymer substrates by sputtering techniques. However, the prospects for development of TCO materials as the active layer in transparent optoelectronic devices [2] have spawned intensive recent interest in the growth of single crystal TCO thin films using techniques such as pulsed laser deposition in clean ultrahigh vacuum systems [3–5], or oxygen plasma assisted molecular beam epitaxy (MBE) [6–17]. Indium oxide (In_2O_3) is a prototypical TCO, which is amenable to degenerate n-type doping with Sn to give so-called indium tin oxide (ITO). In spite of the undoubted technological importance of ITO, many of the basic physical properties of In_2O_3 itself have proved to be controversial, including the nature and magnitude of the band gap [18–20]. For many

[5] Present address: Department of Physics, University of York, Heslington, YO10 5DD, UK.

years the band gap had been presumed to be direct and quoted to be 3.75 eV, a value established by Hamberg *et al* [18]. Band structure calculations [19] are inconsistent with assignment of a weak optical onset observed at 2.69 eV [21] to an indirect gap, but it has recently emerged that there is a lower energy direct but dipole forbidden energy gap that is about 1 eV below this value [8, 20, 22]. An ongoing problem is that it is difficult to obtain high quality In_2O_3 thin films that exhibit intrinsic properties, because native defects almost invariably act as adventitious n-type donors, to the extent that nominally undoped films may in fact support a degenerate electron gas [18]. However, recent improvements in MBE growth procedures have allowed preparation of thin film samples with carrier concentrations well below the limit for the onset of degeneracy, which has been estimated at about 7×10^{18} cm^{-3} [16]. This in turn has led to the realization that the Fermi level at In_2O_3 surfaces is usually pinned around 0.4 eV above the conduction band minimum, so that surface electron accumulation is found for materials with low bulk doping levels, and a distinct conduction band feature appears in photoemission spectra even for doping levels well below that defined by the Mott criterion [8, 16, 22–24]. The ease with which degenerate bulk doping can be achieved, and the downward surface band bending, are both in turn linked to the fact that In_2O_3 has a highly dispersive lower conduction band, but a relatively flat topmost valence band, which leads to a 'charge neutrality level' (that is the mid-gap energy integrated across all k space) that lies above the conduction band minimum [22, 23].

In_2O_3 adopts a cubic bixbyite structure, with space group $Ia\bar{3}$ and lattice parameter $a_e = 10.1170$ Å [25]. The cubic fluorite structure of Y-stabilized ZrO_2 (YSZ) belongs to the space group $Fm\bar{3}m$ with lattice parameter $a_s = 5.1423$ Å at around 17% Y doping level [26]. Note that the subscripts in a_s and a_e denote the substrate and the epilayer respectively. Thus, there is a mismatch of only 1.6% between $2a_s$ for YSZ (10.2846 Å) and a_e for In_2O_3. It is becoming clear that (111) oriented Y-stabilized ZrO_2 is the most promising substrate for heteroepitaxial growth of highly oriented In_2O_3 thin films [4, 5, 12, 14, 16], owing to the fact that the (111) surface of In_2O_3 has the lowest energy amongst the low index surfaces [17]. In the present work, the thickness dependence of the properties of In_2O_3 films grown on Y-ZrO_2(111) is examined in a systematic way, using a combination of experimental and computational methods, and it is shown that there is a clear correlation between film thickness, film morphology and transport properties. It is further shown that ultrathin films are highly strained and that this strain leads to a small but significant reduction in the value of the optical band gap.

2. Experimental details

In_2O_3 thin films with thickness ranging between 35 and 420 nm were grown on 1 cm × 1 cm YSZ(111) substrates (PiKem, UK) in an ultrahigh vacuum oxide MBE system (SVT, USA) with a base pressure of 5×10^{-10} mbar. This incorporated a hot lip indium Knudsen cell and a radio frequency (RF) plasma oxygen atom source operated at 200 mW RF power with an oxygen background pressure of 3×10^{-5} mbar. Substrates were heated radiatively using a graphite filament. The Y-ZrO_2 substrates were cleaned by exposure to the oxygen atom beam at a substrate temperature of 900 °C and all growth runs discussed here were carried out with a substrate temperature of 700 °C. The nominal growth rate was 0.035 nm s^{-1}, which was calibrated using the thickness from high resolution transmission electron microscopy (HRTEM) measurements and atomic force microscopy (AFM) images.

The AFM images were recorded *ex situ* with a Digital Instruments Multimode SPM instrument. This was operated in contact mode with a 'J' scanner having a lateral range of approximately 100 μm and a vertical range of 6 μm. Silicon nitride probes (Nascatec GmbH model NST NCHFR), with a thin coating of gold to act as a mirror for the laser beam, were used. Calibration of the AFM was accomplished by scanning a 10 mm pitch 200 nm 3D reference from Digital Instruments. Digital Nanoscope software (version 5.12) was used to analyse and process the AFM topographic images. All the images were treated with the 'flatten' command and are presented using one of the standard colour palettes of the Nanoscope software.

Specimens for cross-sectional TEM were prepared by cutting and mechanical grinding down to 5–10 μm, followed by thinning to electron transparency by Ar ion beam milling using a Gatan 691 Precision Ion Polishing System (PIPS). Cross-sectional TEM images were collected using a JEOL3000F microscope operating at 300 keV. Digital Micrograph image software was used to process the TEM images. Bragg filtering was applied to the TEM images in order to remove some of the background noise and contrast adjustment was applied uniformly across the images where necessary to enhance the display quality.

3. Computational

To provide an accurate description of the structural, elastic and electronic properties of In_2O_3 under conditions of epitaxial strain, we employed a combination of classical and quantum computational techniques. We have recently developed a pair-wise interatomic potential for In_2O_3 based on the Born model of the ionic solid [27]. The classical electrostatic energy, obtained from an Ewald summation, is combined with a short-range potential of the Buckingham form. The potential model has been successful in describing the high pressure phase transitions of the material [28], in addition to defect formation and diffusion reactions [29]. Full details of the parameterization can be found elsewhere [28]. The pertinent structural and elastic properties resulting from this model for In_2O_3 are collected in table 1, as calculated within the code GULP [30].

In order to obtain information regarding the electronic properties, we have also performed calculations based on density functional theory (DFT) [31, 32]. These calculations were performed using a plane-wave basis set (with a well-converged 500 eV kinetic energy cutoff), within the code VASP [33, 34]. Further details of the computational setup can be found elsewhere [24, 35]. In order to obtain accurate trends

Table 1. Calculated properties of In_2O_3 in the bixbyite mineral structure: a is the cubic lattice constant, ε_0 and ε_∞ are the static and high frequency dielectric constants and C_{ij} are the elastic constants, γ is Poisson's ratio, and E is Young's modulus.

Property	Experiment	Potential model
a (Å)	10.117 [23]	10.121
ε_0^{11}	8.9–9.5 [67]	9.05
ε_∞^{11}	4.0 [67]	3.90
C_{11} (GPa)		297.75
C_{12} (GPa)		141.78
C_{44} (GPa)		76.42
γ		0.323
E (GPa)		206.29

in the material's band gap as a function of epitaxial strain, we have employed a hybrid density functional HSE06 [36, 37], which has demonstrated recent success in describing the electronic properties of oxide materials [38, 39], including the surface work functions of In_2O_3 itself [40]. At this level of theory, the equilibrium lattice constant of $a = 10.156$ Å is within 0.5% of the experimental value.

To simulate the effect of epitaxial strain, the cubic bixbyite lattice was reoriented along the [111] direction using a lattice vector transformation of the form

$$\begin{bmatrix} -1 & 0 & 1 \\ 0 & 1 & -1 \\ 1 & 1 & 1 \end{bmatrix},$$

which results in a hexagonal supercell, in which the epitaxial ($a_e\sqrt{2}$) and uniaxial ($a_e/\sqrt{3}$) lattice constants can be varied independently. The application of strain effectively reduces the lattice symmetry from body centred cubic ($Ia\bar{3}$) to trigonal ($R\bar{3}$). The same lattice expansion is observed for the ordered compound $In_4Sn_3O_{12}$ [41], which could be regarded as very heavily Sn-doped In_2O_3. Importantly, for optical properties, the centre of inversion is maintained for the lattice expansion within the (111) plane.

4. Results and discussion

4.1. Structure and morphology

A low magnification TEM image of a 75 nm thick film viewed down the [1$\bar{1}$0] direction is shown in figure 1(a), revealing a sharp and well defined substrate/epilayer interface. Figure 1(b) shows the corresponding selected area electron diffraction (SAED) pattern taken across the interface, whilst 1(c) is a high resolution TEM image. The near coincidence between the substrate and the epilayer diffraction spots demonstrates the faithful epitaxial relationship between the In_2O_3 film and the YSZ substrate, whilst HRTEM demonstrates an atomically sharp interface.

Figure 2(a) shows a θ–2θ x-ray diffraction trace for a typical thin film sample. Epilayer (222) and (444) reflections appear to a slightly higher angle than the (111) and (222) reflections of the substrate, but no other peaks are observed—the intermediate epilayer (333) reflection is not allowed for a body centred space group. These results confirm that the In_2O_3 films grow epitaxially, with the (111) planes of the epilayer

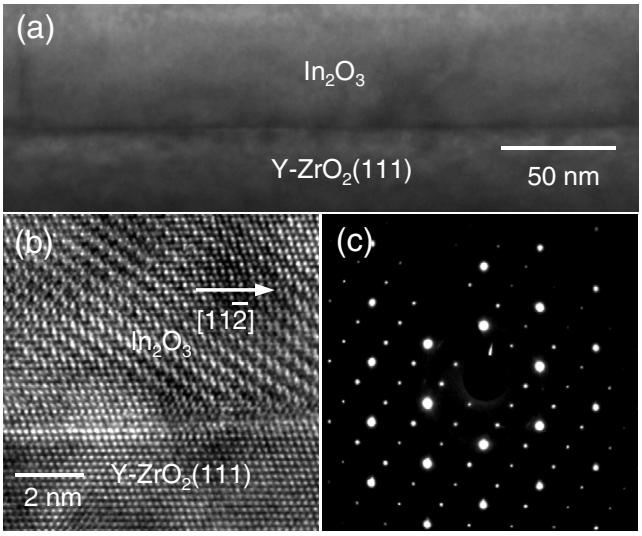

Figure 1. Cross-sectional transmission electron microscopy (TEM) results on an In_2O_3 epilayer on YSZ(111), with a thickness of 70 nm: (a) low magnification image, (b) selected area electron diffraction (SAED) image, and (c) high resolution TEM image viewed down the [1$\bar{1}$0] direction.

parallel to the (111) planes of the YSZ substrate across the complete range of thicknesses studied. Figure 2(b) shows scans across the In_2O_3(222) and YSZ(111) reflections for In_2O_3 films of different thickness. The In_2O_3(222) reflection shifts to lower angle with increasing film thickness, indicating an increase in the out-of-plane d spacing. The change in d spacing can now be explained on the basis that the In_2O_3 film is placed under tensile stress due to the 1.6% mismatch between the YSZ substrate and the In_2O_3 epilayer. The tensile stress gives rise to a lateral expansion in-plane, which in turn leads to a decrease in the interatomic separations normal to the surface. The unit cell in the strained layer is therefore hexagonal rather than cubic, with an in-plane lattice constant $a_\parallel$ that is slightly greater than $\sqrt{2}a_e$ and an out-of-plane constant $c_\perp$ that is slightly less than $a_e/\sqrt{3}$. For a (111) oriented epilayer of a cubic material, the in-plane strain $\varepsilon_{||}$ is related to the out-of-plane strain $\varepsilon_\perp$ through the relationship [42]

$$\varepsilon_\perp = -\varepsilon_\parallel \frac{2C_{12} - 2C_0/3}{C_{11} + 2C_0/3} \quad (1)$$

where

$$C_0 = 2C_{44} - C_{11} + C_{12}. \quad (2)$$

The C_{ij} are the elastic constants of the bulk material. Due to the absence of large single crystal samples, reports on experimental values of the elastic properties of In_2O_3 are scarce. However, using the interatomic potential model that we have developed [28], the three independent elastic constants were calculated as $C_{11} = 297.75$ GPa, $C_{12} = 141.78$ GPa and $C_{44} = 76.42$ GPa and the derived value for C_0 as defined above is -3.13 GPa. It is thus possible to make the estimate

$$\varepsilon_\perp = -\varepsilon_\parallel \times 0.966. \quad (3)$$

Equation (1) can be given in an alternative approximate form:

$$\varepsilon_\perp = -\varepsilon_\parallel \frac{2\gamma}{1-\gamma} \quad (4)$$

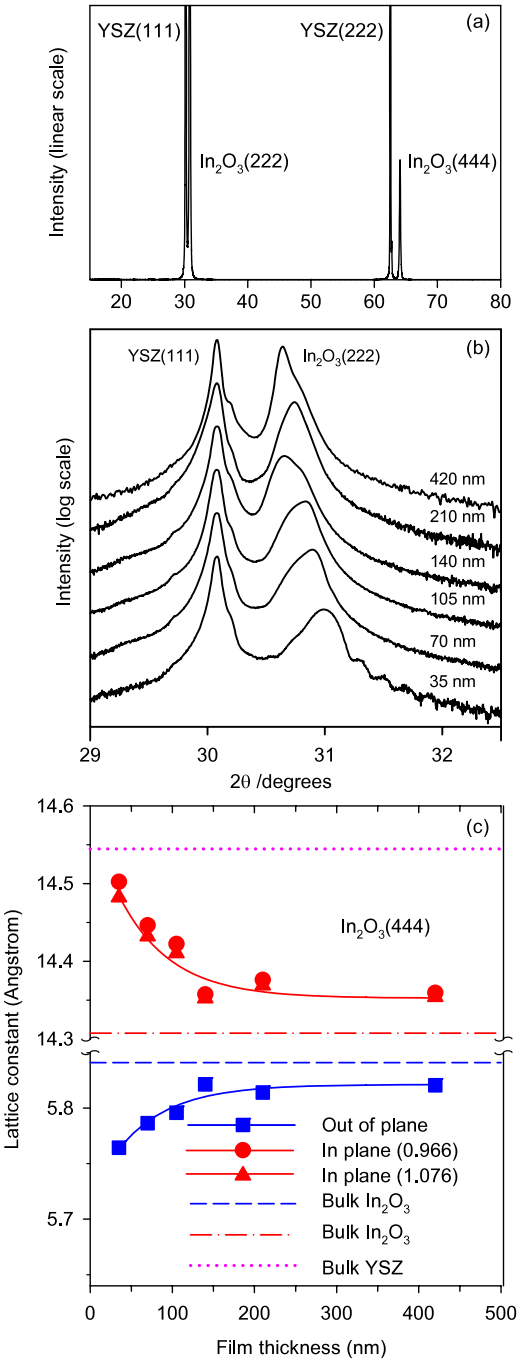

Figure 2. (a) θ–2θ x-ray diffraction profile of In_2O_3. A typical epilayer on Y-stabilised ZrO_2 is presented on a linear scale showing substrate (111) and (222) reflections, along with epilayer (222) and (444) reflections. (b) θ–2θ x-ray diffraction profiles presented on a logarithmic scale of an In_2O_3 epilayer on Y-stabilised ZrO_2 taken across the substrate (111) peak and the epilayer (222) peak as function of film thickness. (c) Out-of-plane ($c_\perp$) and in-plane ($a_\parallel$) lattice constants for epitaxial In_2O_3 obtained from the x-ray diffraction peaks in (b) using the two different values of the ratio between in-plane and out-of-plane strain discussed in the text to derive $a_\parallel$. The corresponding values for the substrate and for the unstrained In_2O_3 are shown as horizontal lines.

where γ is the Poisson ratio. Based on the Poisson ratio determined using our potential model ($\gamma = 0.323$), the uniaxial response remains largely unchanged at 0.954. An empirical estimate of $\gamma = 0.35$ is available from x-ray diffraction data [43], which gives

$$\varepsilon_\perp = -\varepsilon_\parallel \times 1.076. \tag{5}$$

This value is comfortably close to the potential model (within 10%), when one considers that the potential model represents the limit at $T = 0$ K and in the absence of any structural defects. The values of $c_\perp$ obtained from the θ–2θ diffraction profiles along with the derived values of $a_\parallel$ using the two different estimates of the strain ratio are plotted in figure 2(c) as a function of film thickness. The $c_\perp$ values are all lower than the value of $a_e/\sqrt{3} = 5.843$ Å for bulk In_2O_3, although the values for the thicker films come close to this value. Conversely the value for $a_\parallel$ for the thinnest film comes close to matching the substrate value of $2\sqrt{2}a_s$ expected for a coherently strained epilayer. However, even for the thinnest film, the strain does not enable perfect matching. According to Matthews–Blakeslee theory [44], the critical thickness up to which the strained pseudomorphic growth mode with perfect lattice matching can be preserved is around 10 nm for 1.6% mismatch. Thus, even for the thinnest film (35 nm) studied in the current work, one is above this limit. However, from studies of heteroepitaxial III–V systems, it has been suggested that the Matthews–Blakeslee theory underestimates the critical thickness [45]. Indeed, significant lattice relaxation has been found not to occur until layer thicknesses exceed the Matthews–Blakeslee limit by about a factor of ten. When the film thickness is increased to above 140 nm, the residual strain is almost completely relaxed, consistent with this 'Matthews–Blakeslee critical thickness multiplied by ten' rule of thumb.

The surface morphologies of the In_2O_3 films show a pronounced thickness dependence, as seen in the AFM images of figure 3. The film with 35 nm thickness is continuous, with a reasonably flat surface characterized by a root mean square (RMS) roughness of 1.4 nm. The surface is, however, crossed by ridges with a height of 1.8 nm and width of 180 nm running along ⟨110⟩ directions. The ridges intersect each other with a characteristic angle of 60° leading to a so-called 'cross-hatch' surface morphology. Similar morphology has been observed in other heteroepitaxial growth systems with lattice mismatch less than 2%, such as $GaAs_{1-x}P_x$/GaAs [46] and $Si_{1-x}Ge_x$/Si [47–49]. It has been proposed that the cross-hatch patterns are associated with the formation of a network of dislocations at the interface. The 1.6% mismatch between In_2O_3 and YSZ is in the same regime and it is reasonable to conclude that the cross-hatch morphology is again associated with strain relaxation by generation of misfit dislocations. For slightly thicker films, such as the 70 nm film shown in figure 3(b), the density and amplitude of the cross-hatch ridges increase, with a corresponding increase of dislocation density due to the dislocation nucleation and multiplication process [50]. This is consistent with the rapid increase of the out-of-plane lattice constants as the film thickness increases, which has been found in the x-ray diffraction measurements. However, there is still residual strain, and as this accumulates in the In_2O_3 film with further increasing coverage, a 'dewetting' process is favoured [51]. Pinholes or trenches are formed on the surface of a film with nominal thickness of 105 nm, whilst

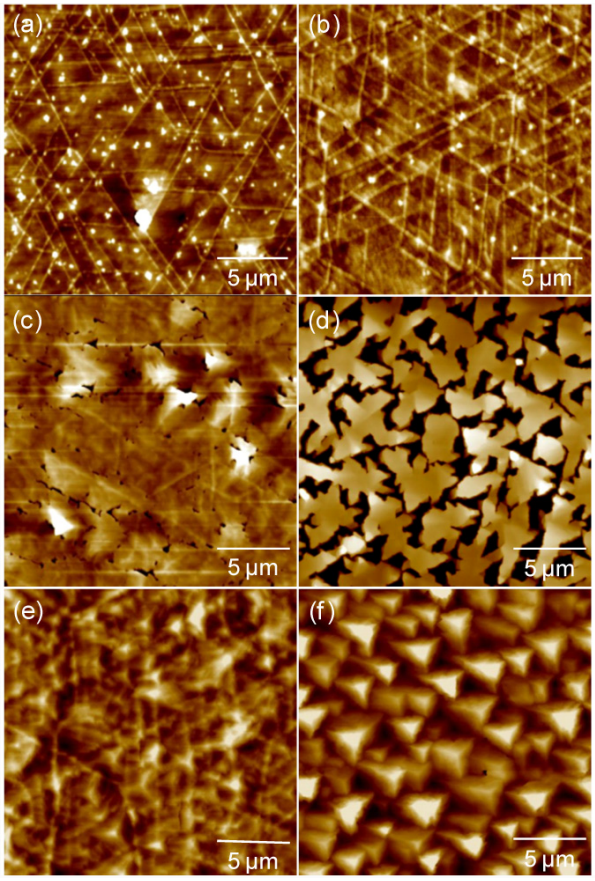

Figure 3. AFM images (20 μm × 20μm) of the surface morphological evolution of the In_2O_3 epilayers on YSZ(111) as a function of film thickness: (a) 35 nm; (b) 70 nm; (c) 105 nm; (d) 140 nm; (e) 210 nm; (f) 420 nm.

after increasing the coverage to 140 nm, the film breaks up into loosely connected mesas with an average size of about 2 μm. The observed 'dewetting' transition from 2D to island-like growth indicates the instability of the 'cross-hatched' structure above a critical thickness. When the coverage is further increased, the In_2O_3 mesas grow laterally and gradually coalesce into a continuous flat thin film with atomic steps. Meanwhile, a sharp unreconstructed $In_2O_3(111)$–(1×1) diffraction pattern is observed with *in situ* low energy electron diffraction (LEED) (image not shown here), indicating the high crystal quality of the thin film after the strain relaxation process.

4.2. Electrical transport properties

The electrical properties of the In_2O_3 films with different thicknesses were characterized by Hall effect measurements using the van der Pauw method at room temperature. Figure 4 shows the Hall mobility and carrier concentration of In_2O_3 thin films as a function of thickness. The 35 nm thick film exhibits the lowest carrier mobility (4.4 $cm^2\ V^{-1}\ s^{-1}$) and highest carrier concentration ($9.1 \times 10^{18}\ cm^{-3}$). The 420 nm thick film shows the highest carrier mobility (73 $cm^2\ V^{-1}\ s^{-1}$) and a very low carrier concentration ($5.0 \times 10^{17}\ cm^{-3}$). The latter is about an order of magnitude lower than the limit for

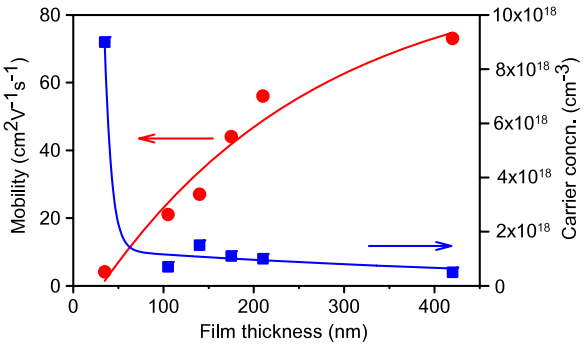

Figure 4. Thickness dependent room temperature carrier mobility and carrier concentration of In_2O_3 films measured by the Hall effect using the van der Pauw method.

the onset of degenerate doping [16]. The optimal mobility is comparable to values of 110 $cm^2\ V^{-1}\ s^{-1}$ reported by Koida and Kondo [5] for In_2O_3 grown on YSZ(111) by pulsed laser deposition, although the adventitious carrier concentration in their work was a factor of ten higher than in the samples grown here. Comparably low doping levels to our own and mobilities of 130 $cm^2\ V^{-1}\ s^{-1}$ were reported by Bierwagen *et al* for In_2O_3 grown on YSZ(001) under In rich conditions [14].

Analysis of the electronic structure, from explicit DFT calculations of the strains of 35 and 420 nm films, reveals that the dispersion in the conduction band does not change significantly when the system is strained: the isotropic electron effective mass ($m^* = \frac{1}{\hbar}\frac{d^2\varepsilon}{dk^2}$) reduces from 0.25 m_e for the bulk material to 0.22 m_e and 0.24 m_e in the 35 and 420 nm mismatched films, respectively. The carrier mobility is proportional to $\frac{1}{m^*}$; however, the small magnitude of the calculated change suggests that the measured change in electron mobility is not determined by a fundamental change in the host band structure. The corresponding band dispersion diagrams are plotted in figure 5.

In heteroepitaxial thin film growth, dislocations are generally in the form of half-loops comprised of a segment of an edge dislocation parallel to the interface and two threading dislocations (TDs), which are inclined or perpendicular the interface [17]. For the thinner In_2O_3 film, a high density of dislocation half-loops is generated within the film in order to release the misfit strain. The dislocation loops may be associated with non-stoichiometric donor defects. The nature of donor defects in In_2O_3 is, however, a controversial issue. The widely presumed assumption that oxygen vacancies act as shallow donors has recently been called into question [52] and the oxygen partial pressure dependence of the donor concentration suggests instead that the donors in sputtered thin films may be singly ionized In–O interstitials [53], that is $(In_i^{\cdots}O_i'')^{\cdot}$ in Kröger–Vink notation; further work to clarify the microscopic nature of the defect chemistry is currently underway. In addition, dislocations may be decorated by interstitial hydrogen, which acts a donor in In_2O_3 and other closely related oxides [54].

The high density of misfit dislocations that must be present in very thin In_2O_3 films acts both as donors and as scattering centres for free electrons, giving rise to low carrier mobility.

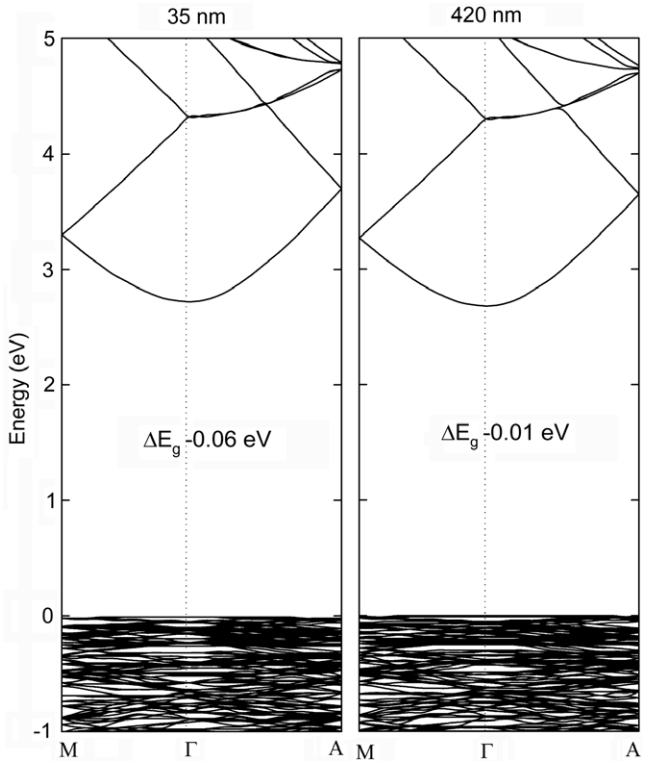

Figure 5. Electronic band structure of (111) epitaxially strained In_2O_3 films, as calculated using density functional theory. The highest occupied state is set to 0 eV. The band gap change is given with respect to the bulk material.

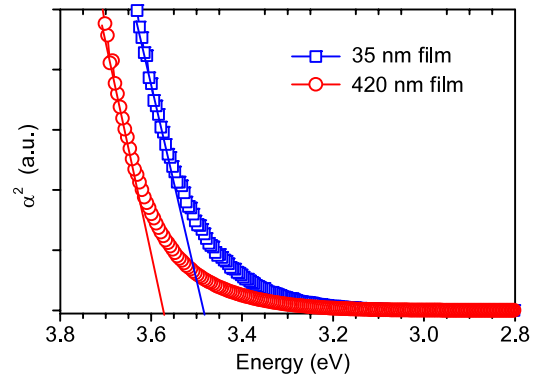

Figure 6. Plot of α^2 against photon energy $h\nu$ for In_2O_3 epitaxial films with thicknesses of 35 and 420 nm. The curves are extrapolated to $\alpha^2 = 0$, in order to determine the effective direct optical band gap.

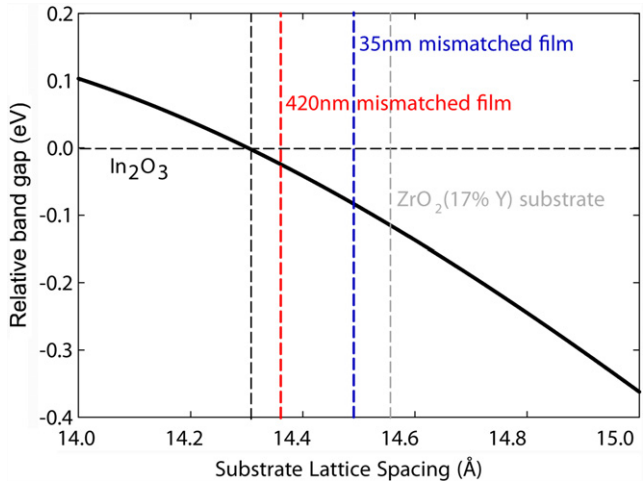

Figure 7. Predicted band gap changes for mismatched In_2O_3 films as a function of the epitaxial lattice spacing, and relative to that of bulk In_2O_3.

As the film thickness increases, the dislocation half-hoops may grow and combine together to form long misfit dislocations at the interface. Strain in the films is gradually relaxed by the formation of misfit dislocations at the In_2O_3/YSZ interface. The threading dislocation density, however, decreases with increasing film thickness due to the combination or mutual annihilation of adjacent threading dislocations. Thus, after the termination of the strain relaxation process, a high quality In_2O_3(111) single crystal film with 420 nm thickness can be fabricated.

Our results show similar trends to those seen in the recent literature on the thickness dependence of the conductivity of epitaxial InN films [55–58]. There, it was found that the carrier concentration dropped from 3×10^{19} cm^{-3} for films with a thickness of about 50 nm to 2×10^{17} cm^{-3} for films of thickness 10 000 nm. At the same time the electron mobility of InN films increased by one order of magnitude from about 300 cm^2 V^{-1} s^{-1} to about 2000 cm^2 V^{-1} s^{-1} [56, 57]. These variations were analysed in terms of a model which identified three parallel contributions to the measured carrier density and mobility. The first was associated with an essentially constant background bulk carrier concentration. The second contribution arose from a surface accumulation layer and the third from an interfacial contribution. The last of these contributions is associated with threading dislocations arising from the misfit strain. It was suggested that the dislocations act as n-type donors and that the average density of the dislocations decays exponentially with increasing InN film thickness.

4.3. Optical band gap

Optical absorption spectra for the thickest and thinnest films prepared in the current experiments are shown in figure 6. They are presented as plots of α^2 versus photon energy $h\nu$, where α is the absorption coefficient. This is the conventional way of using optical data to determine direct allowed energy gaps and is based on the assumption of parabolic bands [59]. The linear extrapolations shown in the figure have intercepts at $h\nu = 3.57$ eV for the film with a thickness of 420 nm, and at $h\nu = 3.49$ eV for the film with a thickness of 35 nm. The optical gap for the thicker film is in general agreement with values reported elsewhere but the small decrease in the band gap for the highly strained 35 nm film is a new observation.

We have also investigated the effect of epitaxial strain on the band gap of In_2O_3 using DFT calculations. The band gap changes are shown in figure 7 for a range of epitaxial lattice spacing; in each case the compensating uniaxial strain is explicitly taken into account. The calculated band gap contraction between the 420 and 35 nm films is 0.06 eV, which compares well to the measured value of 0.08 eV. It

has been established that the electronic and optical band gaps are inequivalent due to optically forbidden transitions from the valence to the conduction bands, arising from the dipole selection rules associated with the spatial inversion symmetry. In the strained material, these selection rules are maintained and the resulting trends in the optical and electronic band gaps are equivalent, i.e. the onset of strong optical transitions still originates from below the top of the valence band.

The observed changes in the band gap arise from the relative energy difference between the valence and conduction bands, but it is instructive to know the absolute contributions in order to understand whether these changes arise from a decrease of the ionization potential or increase of the electron affinity of the material. The effect of isotropic strain can be characterized through the band gap deformation potential characteristic of the material [60]:

$$\alpha_V = \frac{\partial E_g}{\partial \ln V}$$

where E_g is the band gap and V is the unit cell volume. For In_2O_3, we calculate α_V to be -4.21 eV, i.e. compressing the crystal results in a band gap increase. By breaking α_V down into two component absolute deformation potentials for the band edge states, we obtain

$$\alpha_V = \alpha_{\text{conduction band}} - \alpha_{\text{valence band}}$$

where the valence band deformation potential ($\alpha_{\text{valence band}} = -0.10$ eV) is much lower than the corresponding conduction band potential ($\alpha_{\text{conduction band}} = -4.31$ eV). These results demonstrate that the band gap changes in response to lattice strain arise primarily from a change in the electron affinity of the materials. The deformation potential found for In_2O_3 is greater than the values close to -1.7 eV calculated for ZnO [61–65], but less than the estimates of -7 to -8 eV proposed for GaAs and GaN [63, 66]. A deformation potential of -4.21 eV is very close to the values of -3.66 eV [63] and -4.2 eV calculated for InN. Nonetheless, In_2O_3 differs from tetrahedral III–V and II–VI semiconductors in that for the latter $\alpha_{\text{valence band}}$ typically has a positive value that makes a significant contribution to the overall value of α_V. For In_2O_3 the uppermost flat valence bands are relatively insensitive to volume changes.

5. Conclusions

In summary, epitaxial In_2O_3 thin films with thicknesses ranging from 35 to 420 nm were grown on YSZ(111) substrates by oxygen plasma assisted MBE. The tensile strain caused by the 1.6% lattice mismatch was gradually relaxed with increasing film thickness. At the same time it was found that the carrier mobility increased with increasing film thickness. High quality (111) oriented films with a low carrier concentration (5.0×10^{17} cm^{-3}) and high mobility (73 cm^2 V^{-1} s^{-1}) were obtained in the thickest films after strain relaxation. Using a combination of classical and quantum simulation techniques, the uniaxial compression in the response of In_2O_3 to the epitaxial tensile strain was quantified, with the former giving rise to a band gap expansion and the latter to a band gap reduction; the net effect is that for thinner highly mismatched films, the band gap is reduced through a lowering of the conduction band state.

Acknowledgments

We acknowledge useful discussions with Richard Catlow, Scott Woodley and Alexey Sokol. KHLZ would like to thank the Oxford Clarendon Fund for financial support. The Oxford MBE project was initially supported by EPSRC grant GR/S94148. AW would like to acknowledge funding from a Marie-Curie Intra-European Fellowship from the European Union under the Seventh Framework Programme. The computational work has been supported through membership of the UK's HPC Materials Chemistry Consortium, which is funded by EPSRC (Grant No. EP/F067496). TDV acknowledges funding from a Career Acceleration Fellowship from EPSRC (Grant No. EP/G004447/1).

References

[1] Granqvist C G and Hultaker A 2002 *Thin Solid Films* **411** 1
[2] Tsukazaki A, Ohtomo A, Kita T, Ohno Y, Ohno H and Kawasaki M 2007 *Science* **315** 1388
[3] Ohta H, Orita M, Hirano M, Tanji H, Kawazoe H and Hosono H 2000 *Appl. Phys. Lett.* **76** 2740
[4] Ohta H, Orita M, Hirano M and Hosono H 2002 *J. Appl. Phys.* **91** 3547
[5] Koida T and Kondo M 2006 *J. Appl. Phys.* **99** 123703
[6] Taga N, Maekawa M, Shigesato Y, Yasui I, Kakei M and Haynes T E 1998 *Japan. J. Appl. Phys.* 1 **37** 6524
[7] Taga N, Maekawa M, Kamei M, Yasui I and Shigesato Y 1998 *Japan. J. Appl. Phys.* 1 **37** 6585
[8] Bourlange A, Payne D J, Egdell R G, Foord J S, Edwards P P, Jones M O, Schertel A, Dobson P J and Hutchison J L 2008 *Appl. Phys. Lett.* **92** 092117
[9] Bourlange A, Payne D J, Jacobs R M J, Egdell R G, Foord J S, Schertel A, Dobson P J and Hutchison J L 2008 *Chem. Mater.* **20** 4551
[10] Bourlange A, Payne D J, Palgrave R G, Foord J S, Egdell R G, Jacobs R M J, Schertel A, Hutchison J L and Dobson P J 2009 *Thin Solid Films* **517** 4286
[11] Bourlange A, Payne D J, Palgrave R G, Zhang H, Foord J S, Egdell R G, Jacobs R M J, Veal T D, King P D C and McConville C F 2009 *J. Appl. Phys.* **106** 013703
[12] Morales E H, He Y B, Vinnichenko M, Delley B and Diebold U 2008 *New J. Phys.* **10** 125030
[13] Morales E H and Diebold U 2009 *Appl. Phys. Lett.* **95** 253105
[14] Bierwagen O, White M E, Tsai M Y and Speck J S 2009 *Appl. Phys. Lett.* **95** 262105
[15] Bierwagen O and Speck J S 2010 *J. Appl. Phys.* **107** 113159
[16] Zhang K H L *et al* 2009 *Chem. Mater.* **21** 4353
[17] Zhang K H L, Walsh A, Catlow C R A, Lazarov V K and Egdell R G 2010 *Nano Lett.* **10** 3740
[18] Hamberg I, Granqvist C G, Berggren K F, Sernelius B E and Engstrom L 1984 *Phys. Rev.* B **30** 3240
[19] Erhart P, Klein A, Egdell R G and Albe K 2007 *Phys. Rev.* B **75** 153205
[20] Walsh A *et al* 2008 *Phys. Rev. Lett.* **100** 167402
[21] Weiher R L and Ley R P 1966 *J. Appl. Phys.* **37** 299
[22] King P D C *et al* 2009 *Phys. Rev.* B **79** 205211
[23] King P D C, Veal T D, Payne D J, Bourlange A, Egdell R G and McConville C F 2008 *Phys. Rev. Lett.* **101** 116808

[24] Korber C, Krishnakumar V, Klein A, Panaccione G, Torelli P, Walsh A, Da Silva J L F, Wei S H, Egdell R G and Payne D J 2010 *Phys. Rev.* B **81** 165207
[25] Marezio M 1966 *Acta Crystallogr.* **20** 723
[26] Morinaga M, Cohen J B and Faber J 1979 *Acta Crystallogr.* A **35** 789
[27] Born M and Huang K 1956 *Dynamical Theory of Crystal Lattices* (Oxford: Oxford University Press)
[28] Walsh A, Catlow C R A, Sokol A A and Woodley S M 2009 *Chem. Mater.* **21** 4962
[29] Walsh A, Woodley S M, Catlow C R A and Sokol A A 2011 *Solid State Ion.* **184** 52
[30] Gale J D and Rohl A L 2003 *Mol. Simul.* **29** 291
[31] Kohn W and Sham L J 1965 *Phys. Rev.* **140** 1133
[32] Hohenberg P and Kohn W 1964 *Phys. Rev.* **136** B864
[33] Kresse G and Furthmuller J 1996 *Phys. Rev.* B **54** 11169
[34] Kresse G and Furthmüller J 1996 *Comput. Mater. Sci.* **6** 15
[35] Walsh A, Da Silva J L F, Yan Y F, Al-Jassim M M and Wei S H 2009 *Phys. Rev.* B **79** 073105
[36] Heyd J and Scuseria G E 2004 *J. Chem. Phys.* **121** 1187
[37] Heyd J, Scuseria G E and Ernzerhof M 2003 *J. Chem. Phys.* **118** 8207
[38] Marsman M, Paier J, Stroppa A and Kresse G 2008 *J. Phys.: Condens. Matter* **20** 064210
[39] Scanlon D O, Morgan B J, Watson G W and Walsh A 2009 *Phys. Rev. Lett.* **103** 096405
[40] Walsh A and Catlow C R A 2010 *J. Mater. Chem.* **20** 10438
[41] O'Neil D H, Walsh A, Jacobs R M J, Kuznetsov V L, Egdell R G and Edwards P P 2010 *Phys. Rev.* B **81** 085110
[42] Segmuller A 1991 *J. Vac. Sci. Technol.* A **9** 2477
[43] Neerinck D G and Vink T J 1996 *Thin Solid Films* **278** 12
[44] Matthews J W and Blakeslee A E 1974 *J. Cryst. Growth* **27** 118
[45] Bennett B R and del Alamo J R 2002 *Fourth Int. Conf. on Indium Phosphide and Related Materials* p 650
[46] Kishino S, Ogirima M and Kurata K 1972 *J. Electrochem. Soc.* **119** 617
[47] Chen H, Li Y K, Peng C S, Liu H F, Liu Y L, Huang Q, Zhou J M and Xue Q K 2002 *Phys. Rev.* B **65** 233303
[48] Lutz M A, Feenstra R M, Legoues F K, Mooney P M and Chu J O 1995 *Appl. Phys. Lett.* **66** 724
[49] Albrecht M, Christiansen S, Michler J, Dorsch W, Strunk H P, Hansson P O and Bauser E 1995 *Appl. Phys. Lett.* **67** 1232
[50] Hull D and Bacon D J 2001 *Introduction to Dislocations* (Oxford: Butterworth–Heinemann)
[51] Coll M, Gazquez J, Pomar A, Puig T, Sandiumenge F and Obradors X 2006 *Phys. Rev.* B **73** 075420
[52] Lany S and Zunger A 2007 *Phys. Rev. Lett.* **98** 045501
[53] Ohya Y, Yamamoto T and Ban T 2008 *J. Am. Ceram. Soc.* **91** 240
[54] King P D C *et al* 2009 *Phys. Rev.* B **80** 081281
[55] Lebedev V, Cimalla V, Baumann T, Ambacher O, Morales F M, Lozano J G and Gonzalez D 2006 *J. Appl. Phys.* **100** 094903
[56] Piper L F J, Veal T D, McConville C F, Lu H and Schaff W J 2006 *Appl. Phys. Lett.* **88** 252109
[57] King P D C, Veal T D and McConville C F 2009 *J. Phys.: Condens. Matter* **21** 174201
[58] Lebedev V, Cimalla V, Pezoldt J, Himmerlich M, Krischok S, Schaefer J A, Ambacher O, Morales F M, Lozano J G and Gonzalez D 2006 *J. Appl. Phys.* **100** 094902
[59] Pankove J I 1976 *Optical Processes in Semiconductors* (New York: Dover)
[60] Bardeen J and Shockley W 1950 *Phys. Rev.* **80** 72
[61] Janotti A and Van de Walle C G 2007 *Phys. Rev.* B **75** 121201
[62] Zhu Y Z, Chen G D, Ye H G, Walsh A, Moon C Y and Wei S H 2008 *Phys. Rev.* B **77** 245209
[63] Li Y H, Gong X G and Wei S H 2006 *Phys. Rev.* B **73** 245206
[64] Gai Y Q, Yao B, Lu Y M, Shen D Z, Zhang J Y, Zhao D X and Fan X W 2007 *Phys. Lett.* A **372** 72
[65] Li Y F *et al* 2007 *Appl. Phys. Lett.* **91** 021915
[66] Van de Walle C G and Martin R M 1989 *Phys. Rev. Lett.* **62** 2028
[67] Hamberg I and Granqvist C G 1986 *J. Appl. Phys.* **60** R123